Experimental study and numerical simulation of the injection stretch/blow molding process

Fabrice Schmidt, Jean-François Agassant, Michel Bellet

Experimental Study and Numerical Simulation of the Injection Stretch/Blow Molding Process

F. M. SCHMIDT,[1,*] J. F. AGASSANT,[2] *and* M. BELLET[2]

[1]*Ecole des Mines d'Albi-Carmaux*
Campus Jarlard
Route de Teillet
81013 Albi CT Cedex 09, France

[2]*Ecole des Mines de Paris*
CEMEF-URA CNRS no. 1374
06904 Sophia-Antipolis, France

The injection stretch/blow molding process of PET bottles is a complex process, in which the performance of the bottles depends on various processing parameters. Experimental work has been conducted on a properly instrumented stretch/blow molding machine in order to characterize these processing parameters. The objective being a better understanding of the pressure evolution, preform free inflation has been processed and compared with a simple thermodynamic model. In addition, a numerical model for the thermomechanical simulation of the stretch/blow molding process has been developed. At each time step, mechanical and temperature balance equations are solved separately on the current deformed configuration. Then, the geometry is updated. The dynamic equilibrium and the Oldroyd B constitutive equations are solved separately using an iterative procedure based on a fixed-point method. The heat transfer equation is discretized using the Galerkin method and approximated by a Crank-Nicholson's scheme over the time increment. Successful free blowing simulations as well as stretch/blow molding simulations have been performed and compared with experiments.

1) INTRODUCTION

1.1) Presentation of the Study

The injection stretch/blow molding process of poly(ethylene terephtalate) bottles is a three step process (as sketched in *Fig. 1*): first the PET resin is injected in a tube-shaped preform [1], then this amorphous preform is heated above the glass transition temperature [2] and transferred inside a mold. Finally the preform is inflated with stretch rod assistance in order to obtain the desired bottle shape [3].

The performance of PET bottles produced by this process depends on three main processing variables: the initial preform shape, the initial preform temperature, and the balance between stretching and blowing rates. These parameters will induce the thickness distribution of the bottle as well as the biaxial orientation and crystallinity, which in turn governs the transparency and the mechanical properties of the bottle.

This article will deal only with the last step of the process, namely the stretching and blowing phase. Our objective is to propose a general thermomechanical approach that is able to take into account viscoelastic constitutive equations for PET as well as complex boundary conditions. A two-dimensional volumic finite element method has been developed, which is able to capture the shearing effects especially at the contact zone between the moving stretching rod and the preform. Numerical results have been compared with experiments performed on an instrumented stretch/blow molding machine. This model will be a useful tool in order to optimize the processing parameters in order to obtain controlled thickness distribution as well as final stress distribution.

1.2) Literature on Blow Molding Process

A few models have been developed (1, 2) in order to represent heat transfer inside an infrared oven, but because of the complexity of the radiative transfer in a transparent parison, the problem still remains open. A few experimental works refer to the experimental investigation of the kinematics of parison inflation. In several papers (3–6), the authors have recorded the

*Corresponding author.

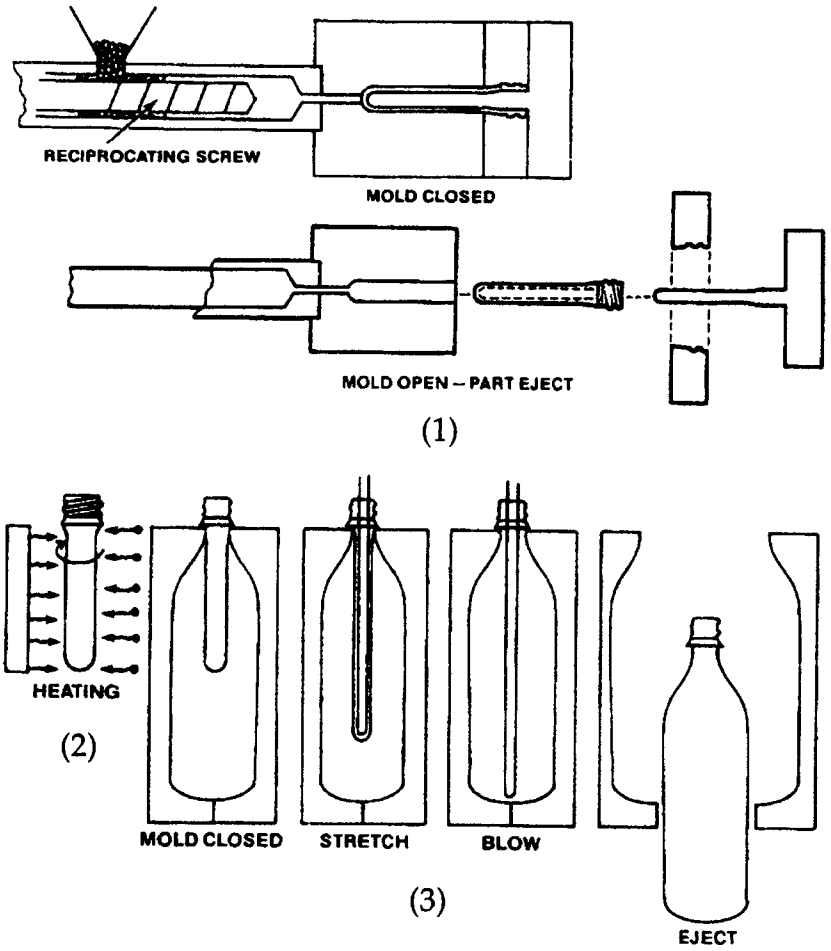

Fig. 1. Description of the injection stretch/blow molding process.

inflation of free (or confined) parisons using high speed video camera. In the case of confined parison inflation, they have designed transparent molds. These works represent an important contribution to the analysis of parison inflation, but the technique still remains limited to simple mold geometries (high curvatures enhance visual distorsions). Experimental work close to the stretch/blow molding process has been performed on a well instrumented machine at Corpoplast company (7): the preform inflation has been investigated using displacement sensors that are located inside the mold, but the force exerted by the polymer on the stretch rod has not been measured.

Finite element numerical simulations of the blow or stretch/blow molding step have been extensively developed during the last decade. Most of the models assume a thin shell description of the parison. Warby and Whiteman (8) as well as Nied *et al.* (9) proposed isothermal finite element calculations. These models, first developed for the thermoforming process, have now been applied to blow molding process. The rheological behavior is approached by a nonlinear-elastic constitutive equation issued from the rubber-like materials theory. Kouba *et al.* (10) extended the previous model to a viscoelastic fluid (KBKZ constitutive equation). Several models use a volumic finite element approach. In 1986, Cesar de Sa (11) simulated the blowing process of glass parisons assuming an Arrhenius temperature dependent Newtonian behavior. Chung (12) carried out simulations of the PET stretch/blow molding process using the ABAQUS® software. The model assumes the elasto-visco-plastic behavior and thermal effects are neglected. Poslinski *et al.* (13) introduced nonisothermal effects in a simplified geometry. In order to take into account the phase change, the latent heat of solidification was included in the heat capacity of the material. Debbaut *et al.* (14) also performed nonisothermal viscoelastic blow molding simulations with a Giesekus constitutive equation, but they presented numerical results only in the case of a Newtonian fluid.

In conclusion, the thin shell assumption, which permits 3D finite element computations, is often used and commonly associated to the hyperelastic behavior issued from solid elastic media. The finite element volumic approach issued from the blow molding of glass parisons is generally employed with liquid-like constitutive equations (Newtonian, viscoelastic) and is limited to 2D computations. In the stretch/blow molding step, the contact between the stretch rod and the bottom of the preform induces shear deformations as well as high and localized temperature gradients,

which actually justify a volumic approach in order to obtain an accurate description of the deformation.

2) EXPERIMENTAL INVESTIGATIONS

2.1) Instrumented Mold of a Stretch/Blow Molding Machine

Experiments were performed on a well-instrumented mold at the Sidel Company (15). The dimensions of the preform and of the mold are summarized in *Table 1*. The instrumentation is described in *Fig. 2*: the displacement of the stretch rod is controlled and the force exerted on the stretch rod is recorded versus time using a force sensor. The blowing pressure is recorded versus time using a pressure sensor (the pressure value is actually different from the imposed blowing pressure). Nine contact sensors at the mold wall permit to identify the contact time between the polymer and the mold.

The parameters associated with the stretching stage are the velocity of the stretch rod v_c, which is applied until the preform contacts the bottom of the mold, and the preblowing step (*Rps* = displacement of the stretch rod before the inflation pressure is imposed). The parameters associated with the inflation stage are *Pps*, the maximum pre-blowing pressure (low-pressure) imposed during a preblowing time *Dps* for initiating the general shape of the bottle, and *Ps*, the maximum blowing pressure (high-pressure) that is applied during a blowing time *Ds* in order to flatten the polymer along the mold wall. The preblowing air-rate *Qps* and the blowing air-rate *Qs* are prescribed by the operator but not measured.

Typical values of the process parameters of the stretch/blow molding step are referred in *Table 2*. The

Table 1. Dimensions of the Bottle Mold and the Preform.

	Length (mm)	Inner Radius (mm)	External Radius (mm)
Preform	125	9.275	13.025
Bottle mold	310	44.3	44.3

Table 2. Processing Parameters.

Stretching stage	v_c (mm/s)	500
	R_{ps} (mm)	1
Preblowing stage	P_{ps} (Pa)	5×10^5
	D_{ps} (s)	0.3
	Q_{ps} (kg/s)	—
Blowing stage	P_s (Pa)	40×10^5
	D_s (s)	1.5
	Q_s kg/s)	—

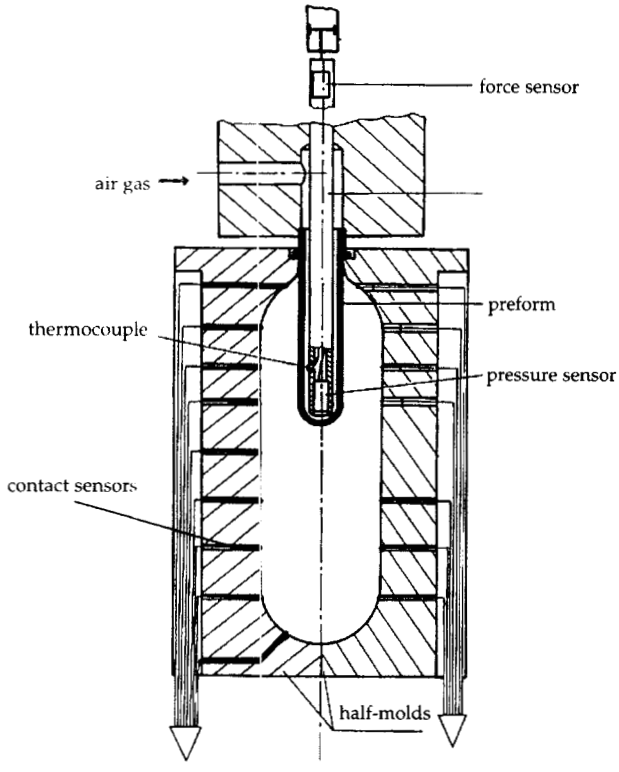

Fig. 2. Description of the instrumented mold of a stretch/blow molding machine.

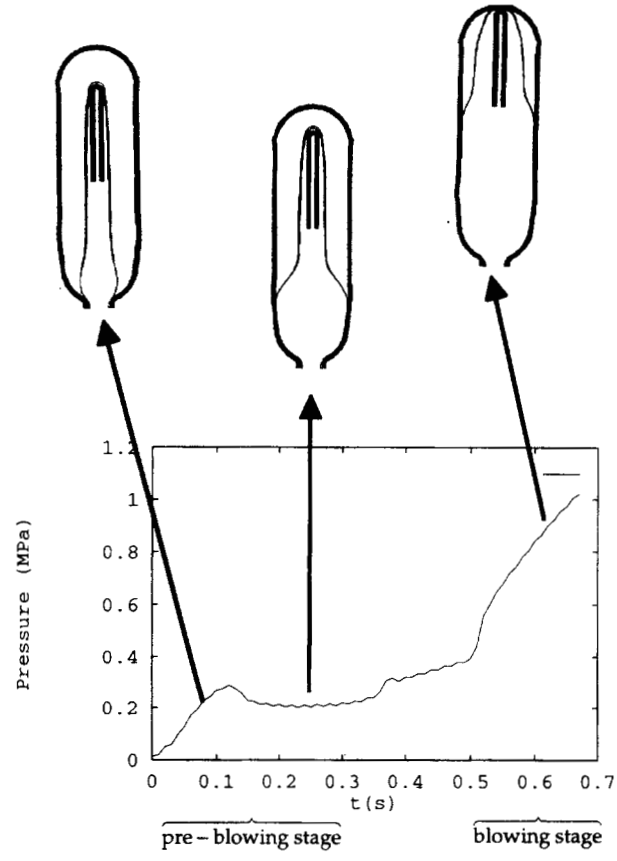

Fig. 3. History of pressure versus time.

pressure is measured directly in the preform (see *Fig. 3*). In addition, short-shot bottles produced for the target process are time-located on the recorded pressure curve.

As shown in *Fig. 4*, the measured stretching force of the rod versus time starts from zero (or from a very low value), and then the curve rises to a maximum and decreases continuously. Note that when *Rps* increases, the maximum of the curve increases. In previous papers (16, 17), we pointed out that the increasing part and the decreasing part of this curve may be related respectively to elastic and viscous phenomena.

The location of the contact sensors (from n° 1 to n° 9) on the mold wall is indicated in *Fig. 5*. Recorded contact times versus the location of contact sensors are plotted in *Fig. 6* using the process parameters that are referred in *Table 2*. When the preblowing delay *Rps* is increased from 1 mm to 40 mm, all the contact times between the polymer and the mold increase and the contact times are more homogenous in the central part of the bottle. In addition, if we plot the measured thickness distribution versus longitudinal coordinate at the end of the process for the two values of *Rps* (see *Fig. 7*), we note that an increase in the preblowing

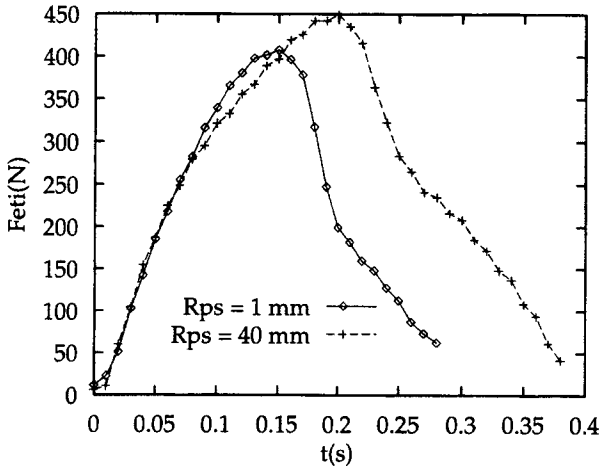

Fig. 4. Measured stretching force of the rod versus time.

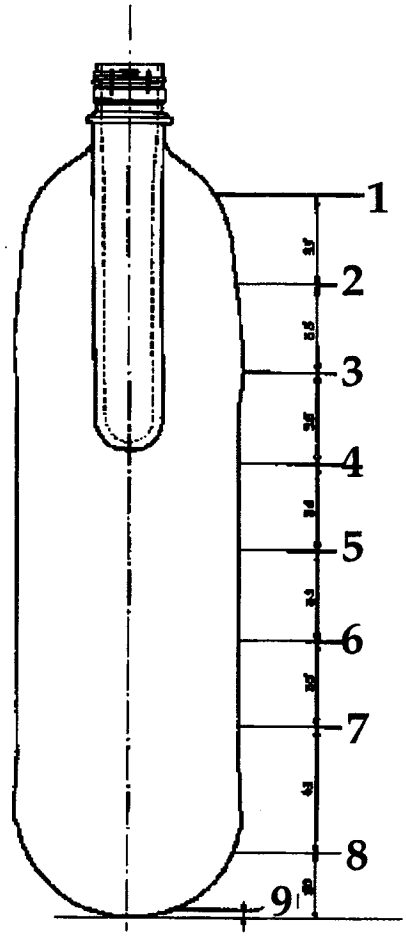

Fig. 5. Location of the contacts sensors on the mold wall.

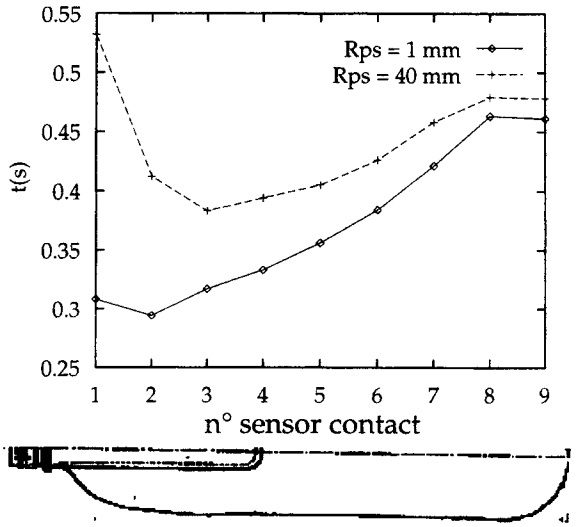

Fig. 6. Contact times versus number of contact sensors.

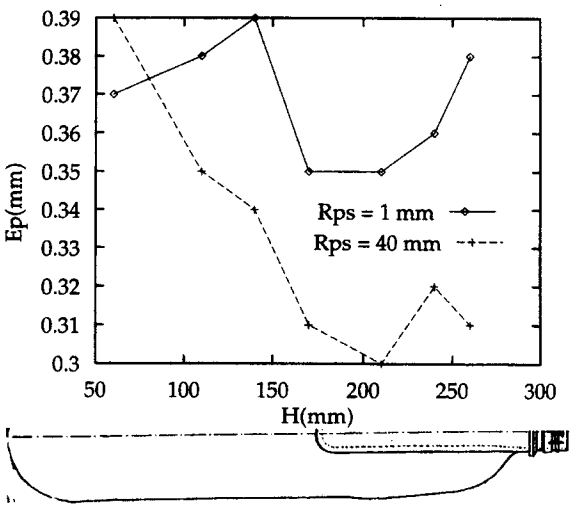

Fig. 7. Thickness distribution at the end of the process.

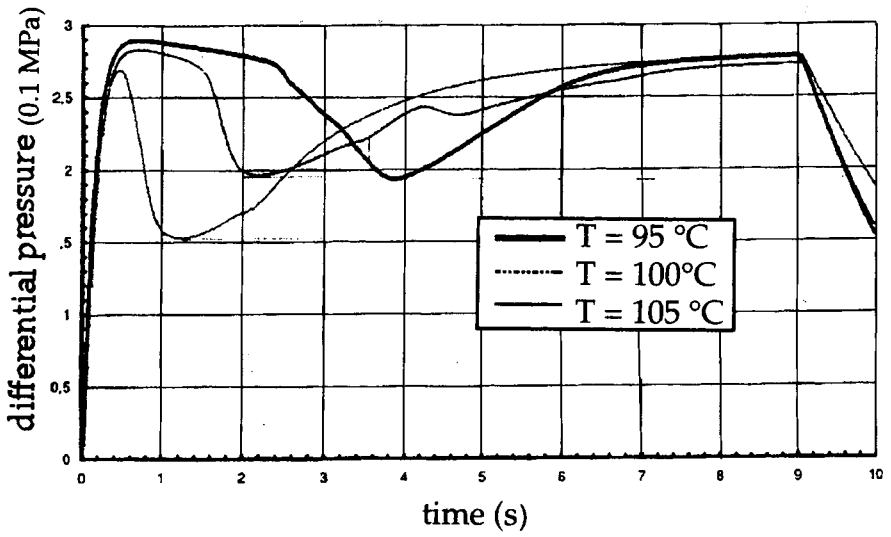

Fig. 8. Differential pressure vs. time.

delay induces more material displacement from the neck to the bottom of the bottle.

2.2) Measurement and Calculation of the Internal Pressure

In fact, in industrial blowing tools, the inflation pressure is only imposed and measured in the blowing device upstream and not inside the preform; significant differences may be observed between these two pressures. Let us consider now the free inflation of a preform. The preform is heated in a silicone oil bath in order to obtain a uniform temperature distribution (T = 95°C, 100°C, 105°C). A "nominal" pressure has been imposed to a constant value of 0.27 MPa in the upstream blowing device for each case and the differential inflation pressure $\Delta p_a(t) = p_a(t) - p_o$ ($p_a(t)$ inflation pressure, p_o atmospheric pressure at ambient temperature) is recorded versus time using a pressure sensor (see *Fig. 8*). For each temperature, free inflations were recorded using video camera. In *Fig. 9*, successive preforms during free inflation are presented at T = 105°C. Three different parts may be observed on each curve:

- a first part where the pressure rises to a maximum (less than 0.3 MPa), during which the polymer is not inflated (the internal volume of the preform remains constant);
- a second part where the pressure decreases continuously to a minimum because the volume increases;
- the last part of the curve where the pressure increases again because of the "strain-hardening" of the material, which is in fact related to the development of crystallinity under biaxial stretching.

It is to be noted that the duration of these three steps during free inflation is strongly dependent on temperature. This experiment demonstrates that the evolution of the internal pressure and the inflation of the preform are highly coupled. It is also to be noted that the recorded internal pressure is significantly different from the "nominal" pressure. In order to better understand this pressure evolution, we develop hereafter a simple thermodynamic model. As sketched in *Fig. 10*, we consider that air flows in the "control volume" $V_a(t)$ at an air-rate q with a velocity field, pressure p_e and a temperature T_e. We assume that the air-rate q is constant during the pre-blowing stage, which results in the following relationship between the air mass $m_a(t)$ (occupying the volume $V_a(t)$) and q:

$$q = \frac{dm_a}{dt} = cte \Rightarrow m_a(t) = m_o + qt \qquad (1)$$

where m_o is the air mass within the parison at time $t = 0$. Using the following assumptions:

- no heat transfer between the air volume and the surrounding medium,
- air is an ideal gas,

the global energy balance during the time step dt over the volume $V_a(t)$ may be simplified as (18):

$$\frac{d}{dt}\left(Ln(p_a V_a^{\gamma})\right) = \frac{d}{dt}\left(Ln(m_a^{\gamma})\right)\frac{T_e}{T_a} \qquad (2)$$

where $\gamma = 1.4$ for air. In order to obtain a simplified relationship, we assume $T_a \cong T_e$, which is consistent with the assumption of no heat transfer with the surrounding medium. Using *Eq 1* and $m_a = \rho_a V_a$, *Equation 2* reduces to:

$$\frac{p_a(t)}{p_o} = \frac{1}{\rho_o^{\gamma}}\left(\frac{m_o + qt}{V_a(t)}\right)^{\gamma} \qquad (3)$$

where ρ_o is the air specific mass at time $t = 0$ (initial ambient temperature). Knowing the volume $V_a(t)$ (due to parison inflation), this relation should provide the pressure value $p_a(t)$. However, the experimental determination of the air-rate q is very difficult. In order to overcome this difficulty, we suggest that q should be determined through an inflation test at constant volume V_o (for example, using a preform which has not been heated). Differentiating *Eq 3* with respect to time,

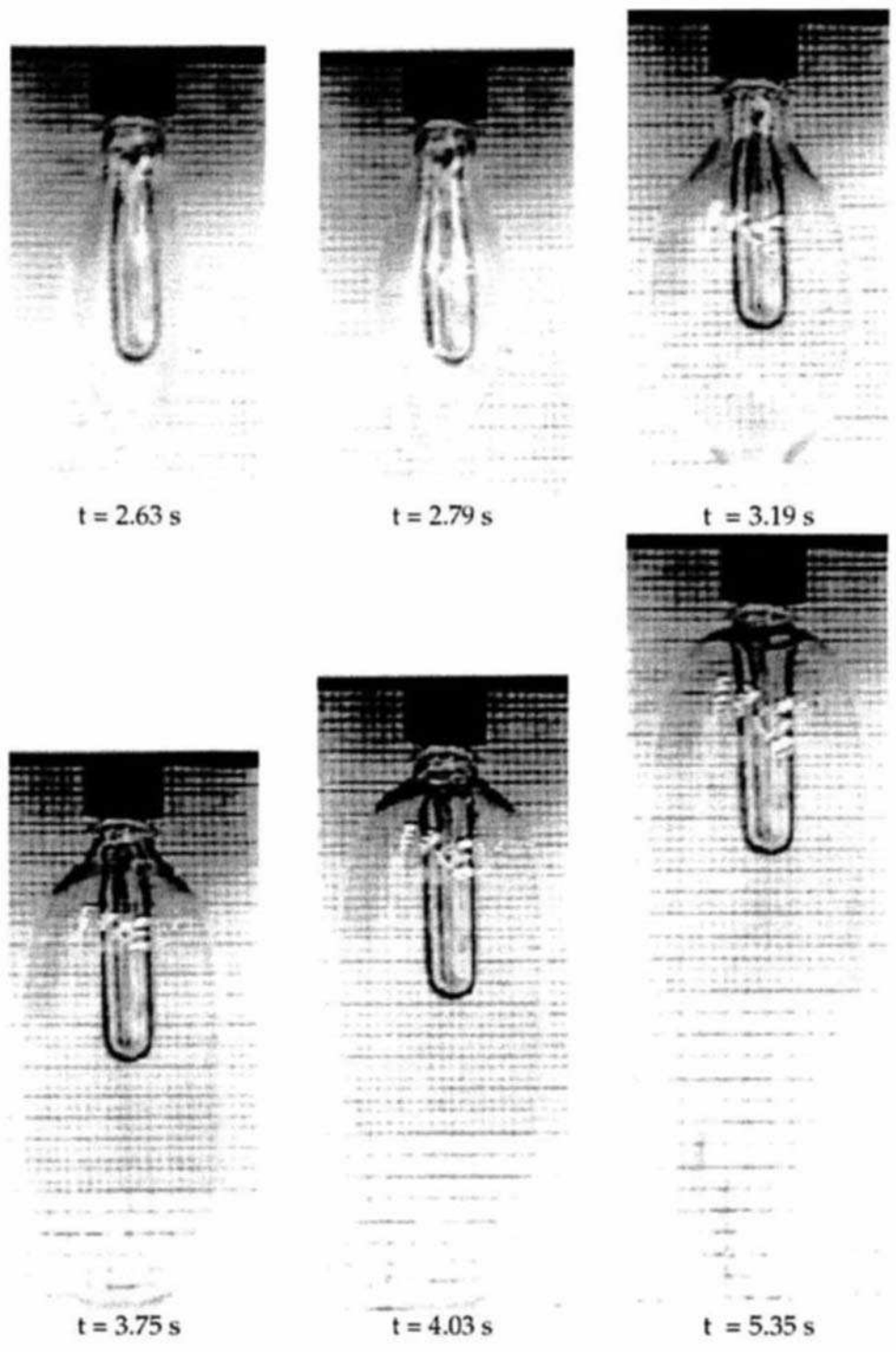

Fig. 9. Preform free inflation (T = 105°C).

we obtain at initial time $t = 0$:

$$q = \frac{\rho_o V_o}{\gamma p_o} \left.\frac{dp_a(t)}{dt}\right|_{t=0} \quad (4)$$

Once the specific flow-rate q (or $\left.\frac{dp_a(t)}{dt}\right|_{t=0}$) has been experimentally determined, it is possible to express the inflation pressure $\Delta p_a(t)$:

$$\frac{\Delta p_a(t)}{p_o} = \left(\frac{V_o}{V_a(t)}\right)^{\gamma} \left(1 + \frac{t}{\gamma p_o} \left.\frac{dp_a(t)}{dt}\right|_{t=0}\right)^{\gamma} - 1 \quad (5)$$

This relationship has been introduced in the stretch/blow molding finite element software BLOWUP (18). Results will be presented in *Section 5*. $\Delta p_a(t)$ will be determined as follows:

- inflation at a given flow-rate of a preform that has not been heated and measurement of the initial slope of the recorded pressure curve,

• calculation of the initial internal volume of the preform V_o,

• computation of the internal volume of the preform $V_a(t)$ at each time step,

• determination of $\Delta p_a(t)$ using *Eq 5*.

3) BOUNDARY CONDITIONS

The boundary conditions are presented in *Fig. 11*:

• along the contact surface between the rod and the preform

$v = v_c$ (sticking contact)
$T = T_r$ (prescribed temperature at the rod; note that the temperature of the rod is not easy to measure)

• along the internal surface of the preform, which is not in contact with the rod

$$(\sigma \cdot \vec{n}) \cdot \vec{n} = -\Delta p_a(t)$$

$$(k\nabla T) \cdot \vec{n} = -h_a(T - T_a)$$

where h_a is the heat transfer coefficient between the polymer and the air inside the parison; however, the extracted heat flux can be generally neglected.

• along the external surface of the preform, which is in contact with the mold

$v = 0$
$T = T_m$ (prescribed temperature of the mold)

• along the external surface of the preform, which is not in contact with the mold

$$(\underline{\sigma} \cdot \vec{n}) \cdot \vec{n} = 0$$

$$(k\nabla T) \cdot \vec{n} = -h_m(T - T_m)$$

where h_m is the heat transfer coefficient with the mold, which will vary continuously during the inflation process.

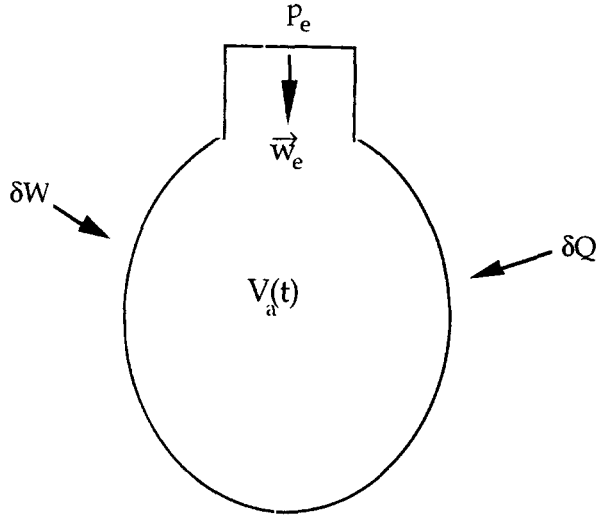

Fig. 10. Volume free blowing at a constant flow rate.

4) NUMERICAL RESOLUTION

4.1) Thermomechanical Equations

The numerical simulation of the stretch/blow molding of an incompressible viscoelastic fluid (Oldroyd B type) consists in solving the following set of equations on the domain Ω occupied by the preform:

$$\rho(\vec{\gamma} - \vec{g}) = \nabla \cdot \underline{\sigma} \quad \text{where } \underline{\sigma} = -p'\underline{I} + 2\eta_s\underline{\dot{\varepsilon}} + \underline{\tau} \tag{6}$$

$$\nabla \cdot \vec{v} = 0 \tag{7}$$

$$\underline{\tau} + \lambda \frac{\delta \underline{\tau}}{\delta t} = 2\eta_v \underline{\dot{\varepsilon}} \tag{8}$$

$$\rho c_p \frac{dT}{dt} = \nabla \cdot (k\nabla T) + \underline{\sigma} : \underline{\dot{\varepsilon}} \tag{9}$$

with the above-mentioned boundary conditions. In this model, the mechanical equations (*Eqs 6 to 8*) and the temperature balance equation (*Eq 9*) are solved separately on the deformed configuration Ω^n at current time step t_n (see *Fig. 12*). The current values of the velocity vector $\vec{v}^n$, the pressure p'^n and the extra-stress tensor $\underline{\tau}^n$ are determined first. Then the temperature field T^{n+1} is computed. Finally, the geometry is updated from Ω^n to Ω^{n+1} using the 2nd order explicit Euler rule:

$$\vec{x}^{n+1} = \vec{x}^n + \Delta t_{n+1} \cdot \vec{v}^n + \frac{\Delta t_{n+1}^2}{2} \cdot \left(\frac{\vec{v}^n - \vec{v}^{n-1}}{\Delta t_n} \right) \tag{10}$$

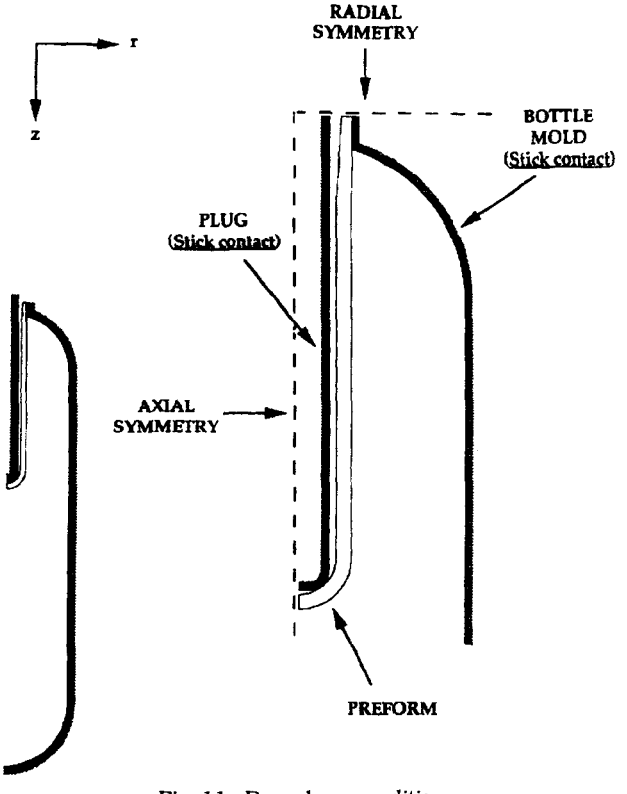

Fig. 11. Boundary conditions.

4.2) Resolution of the Mechanical Equations

The resolution method is summarized hereafter. Full details about the numerical algorithms are given elsewhere (16, 17).

4.2.1) Splitting Technique

At each time step, an iterative procedure based on a fixed-point method is used in order to solve *Equations 6* to *8*. The first sub-problem, called the "Generalized Stokes Problem" (GSP), deals with an incompressible Newtonian fluid flow, perturbed by a known extra-stress tensor $\underline{\underline{\tau}}^n$ computed at the previous fixed-point iteration (fix-1) (*Equations 6* and *7*). The second sub-problem consists in determining the components of the extra-stress tensor $\underline{\underline{\tau}}^n$ for a known velocity field by solving the time-discretized constitutive equation (*Eq 8*). The procedure is repeated until convergence.

4.2.2) Spatial Discretization

The domain Ω is approximated by a set of 6-node isoparametric triangles T^h (quadratic element, see *Fig. 13*), which are defined by the shape functions $\vec{N}_k$. The nodal velocity field is expressed in term of the component v_k of the nodal velocity vectors with the same shape functions. The pressure is constant by element. Using the Galerkin method, the discretized equations of GSP at current time t_n lead to the following system:

$$\begin{cases} A\vec{V} + {}^tB\vec{P} = \vec{F} & (11) \\ B\vec{V} = 0 & (12) \end{cases}$$

where the matrix A, B and the vectors $\vec{V}, \vec{P}, \vec{F}$ are given elsewhere (16). In order to find $\vec{V}, \vec{P}$, we use an iterative scheme derived from Uzawa's algorithm (16). The bounded set of linear algebraic equations is solved by a direct Crout decomposition.

4.2.3) Viscoelastic Equation

As the different integrals in *Equation 11* are evaluated by the Gauss-Legendre point integration rule, the components of the current extra-stress tensor $\underline{\underline{\tau}}^n$ are needed only at the Gaussian points of each element. Consequently, the tensorial equation (*Eq 8*) is solved at a local level; it reduces to a (4 × 4) linear algebraic system.

$$K_v(\vec{\tau}_v) \cdot \vec{\tau}_v = \vec{R}_v \qquad (13)$$

where the matrix K_v and the vectors $\vec{\tau}_v$, $\vec{R}_v$ are defined elsewhere (18). The set of linear algebraic equations (Eq 13) is solved by a direct Gauss method.

4.3) Thermal Balance Equation

The time differential equation (*Eq 9*) is approximated by a Crank-Nicholson's scheme over the time in-

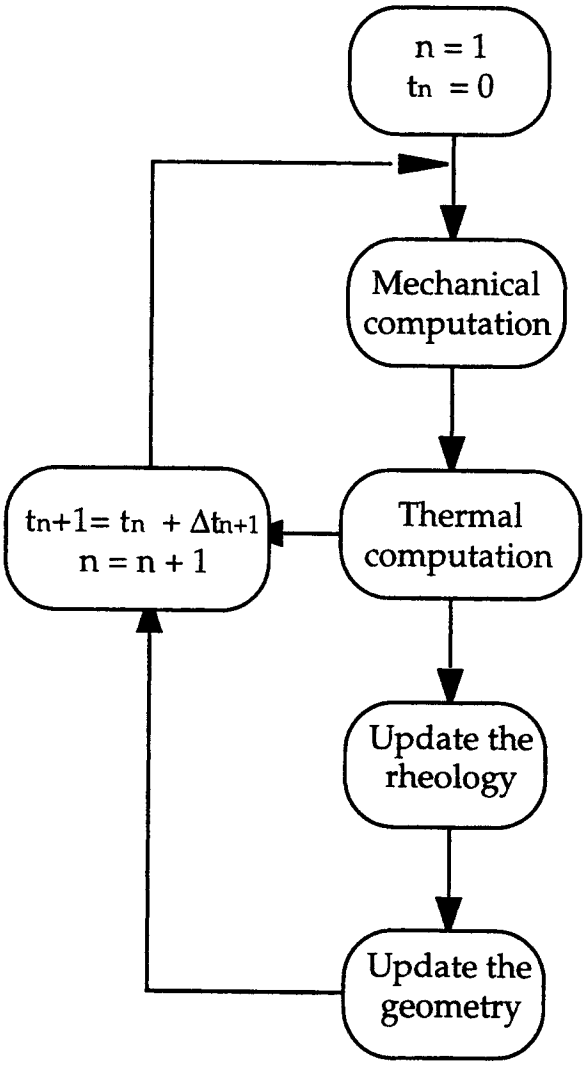

Fig. 12. Thermomechanical algorithm.

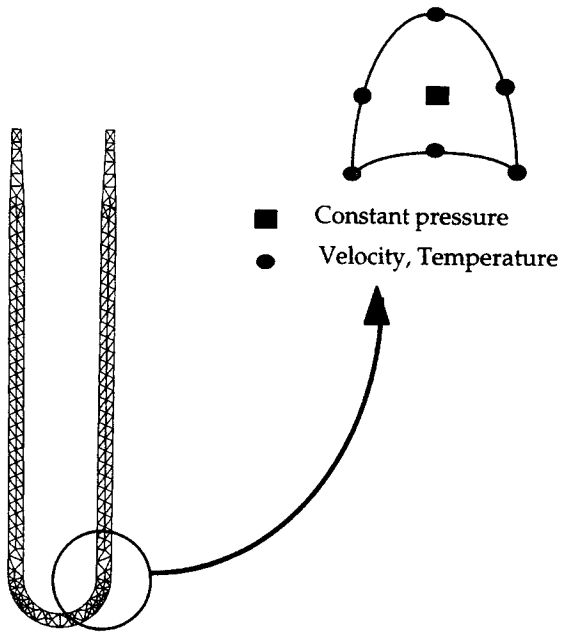

Fig. 13. Mesh of the preform and P2-P0 element.

crement Δt_n. Using Galerkin method, the discretized equation (*Eq 9*) at current time t_n leads to the following system:

$$C^*\left(\frac{\vec{T}^{n+1}-\vec{T}^{n}}{\Delta t_n}\right)+K^*\left(\frac{\vec{T}^{n+1}+\vec{T}^{n}}{2}\right)+\vec{S}^*=0 \qquad (14)$$

The capacity matrix C, the conductivity matrix K, and the vectors $\vec{T}, \vec{S}$ are defined below:

$$\vec{T}=(T_1,\ ...,\ T_k,\ ...,\ T_{Ntnoe})$$

$$\begin{cases} C_{kl}=\int_{\Omega}\rho C_p\,\Psi_k\Psi_l\,d\nu \\ K_{kl}=\int_{\Gamma_a}h_a\,\Psi_k\cdot\Psi_l\,dS+\int_{\Gamma_m}h_m\,\Psi_k\cdot\Psi_l\,dS \\ \qquad\qquad +\int_{\Omega}k\nabla\Psi_k\nabla\Psi_l\,d\nu \\ S_l=-\int_{\Gamma_a}h_a\,T_a\cdot\Psi_l\,dS-\int_{\Gamma_m}h_m\,T_m\cdot\Psi_l\,dS+\int_{\Omega}\dot{W}\Psi_l\,d\nu \end{cases}$$

Each matrix M^* (= C^*, K^*, $\vec{T}^*$) takes the following form:

$$M^*=\frac{3}{2}M^n-\frac{1}{2}M^{n-1} \qquad (15)$$

which results from a linearized technique (19) in order to avoid an iterative resolution of *Eq 14*. Only the nonreversible part of the stress tensor $\underline{\sigma}|_v$ (viscous part) contributes to the dissipated energy $\dot{W}$.

$$\dot{W}=\underline{\sigma}|_v:\underline{\dot{\varepsilon}}=2(\eta_s+\eta_v)\,\underline{\dot{\varepsilon}}:\underline{\dot{\varepsilon}}=2\eta\,\underline{\dot{\varepsilon}}:\underline{\dot{\varepsilon}}$$

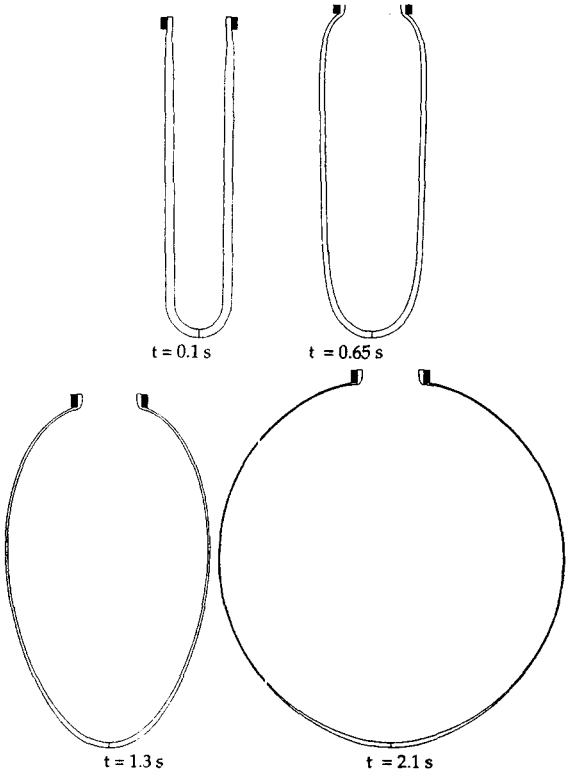

Fig. 14. Intermediate bubble shapes (T = 105°C).

Table 3. Processing and Rheological Parameters for Free Inflation at T = 105°C.

Process Parameters			Rheological Parameters		
Maximum pressure (bars)	T (°C)	$\frac{dP(t)}{dt}\Big\|_{t=0}$ (MPa/s)	η_s (MPa.s)	η_v (MPa.s)	λ(s)
2.7	105	2.58	0.0123	0.27	0.1

The linear system (Eq 14) is solved by a direct Crout decomposition.

4.4) Variation of Viscosity With Temperature

The empirical relation proposed by Ferry *et al.* (20) accounts for rapid variation of the viscosity between the glass transition T_g and T_g + 100°C.

$$\frac{\eta(T)}{\eta_g}=\frac{T}{T_g}\frac{\rho}{\rho_g}e^{\frac{-C_1^g(T-T_g)}{T-T_g+C_2^g}} \qquad (16)$$

where $C_1^g = 8.38\ K^{-1}$ and $C_2^g = 42.39\ K$ (21).

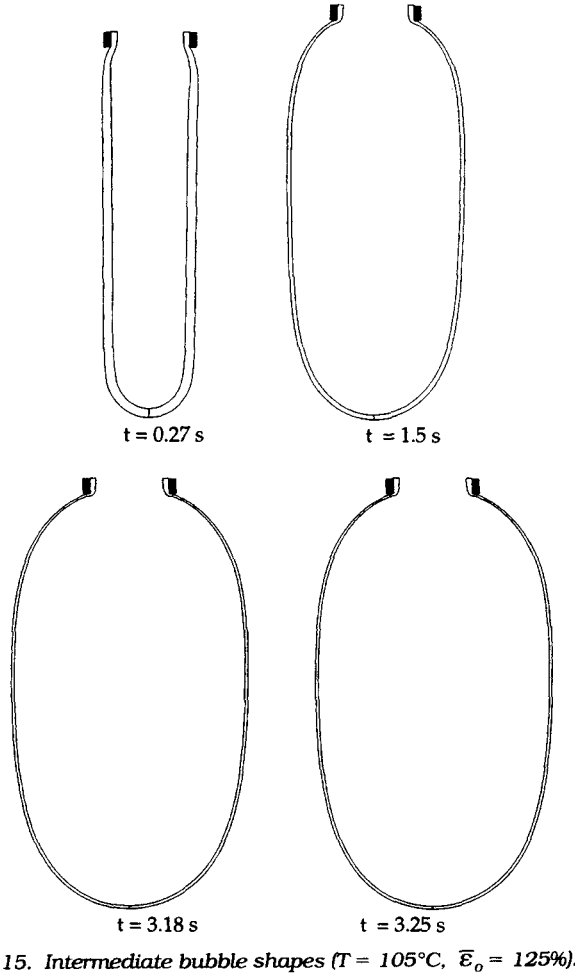

Fig. 15. Intermediate bubble shapes (T = 105°C, $\bar{\varepsilon}_o$ = 125%).

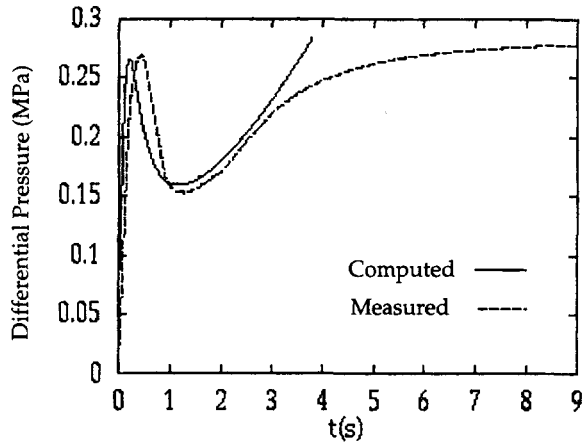

Fig. 16. Differential inflation pressure versus time.

5) APPLICATIONS

5.1) Preform Free Inflation

Let us proceed to free inflation simulations at T = 105°C in order to compare the computed differential inflation pressure to the measured one (see **Section 2.2**). Processing parameters are given in *Table 3*. Viscoelastic parameters have been adjusted in order to obtain the same maximum pressure. We assume that the relaxation time remains constant. It appears immediately in *Fig. 14* that the expansion of the preform and especially the radial expansion is unlimited. This problem, which is not observed experimentally, occurs because the strain-hardening phenomenon of the material, related to the development of crystallinity under biaxial stretching, is not taken into account in the numerical model, and this problem has not been addressed in this paper. Introducing a viscosity dependent on the generalized strain $\bar{\varepsilon} = \int_0^t \sqrt{\frac{2}{3}\,\dot{\varepsilon}_{ij}\,\dot{\varepsilon}_{ij}}$ as proposed by G'Sell (22):

$$\eta = \eta_0(T)\,.exp\left(\frac{\bar{\varepsilon}}{\bar{\varepsilon}_0}\right)^2$$

↑ *WLF* ↑ *strain – hardening*

where $\bar{\varepsilon}_o$ is a reference value, leads to limit the expansion of the preform (see *Fig. 15*). In that case, the computed differential inflation pressure and the measured one are plotted in *Fig. 16*. We note that the agreement is fair between the two curves except in the

Table 4. Rheological Parameters for Stretch/Blow Molding.

T_g (°C)	η_s (MPa.s)	η_v (MPa.s)	λ(s)
84.2	0.05	2.5	0.1

Table 5. Typical Values for the Physical Propertiesfor the PET.

Physical Properties	Typical Value
ρ (kg/m³) at T_g = 80°C	1336
k (W/m.K)	0.25
C_p (kJ/kg.K)	
at 23°C	1.13
at 80°C	1.42
at 100°C	1.51
at 200°C	1.88

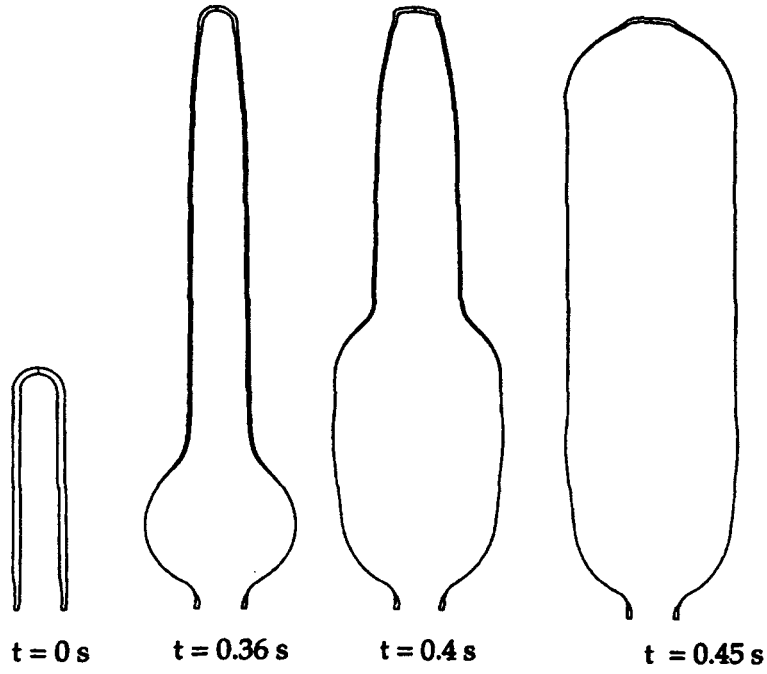

Fig. 17. Intermediate bottle shapes.

last part. The computed preform inflation remains, however, significantly different from the free inflation that has been recorded using video camera (*Fig. 9*).

5.2) Setup of a Real Stretch/Blow Molding Process

We study now a stretch/blow molding operation. The geometries of the bottle mold and of the preform, the processing parameters have been previously referenced in *Fig. 5*, *Table 1*, and *Table 2*, respectively (see **Section 2.1**). The initial mesh of the preform has been shown in *Fig. 13*. For this thermomechanical simulation, we use the experimental pressure that has been plotted in *Fig. 3* (i.e. the pressure is not calculated using *Eq 5*). The viscoelastic rheological parameters (*Table 4*) have been determined by fitting on the traction force of an amorphous PET sample, injected in the same conditions as the tube shaped preform (18). Typical values for the physical properties of the PET are referenced in *Table 5*. The value of the heat transfer coefficient between the air and the polymer is considered to be h_a = 10 W/K.m^2. A high value for the heat transfer coefficient between the mold and the polymer h_m = 500 W/K.m^2 has been applied at the interface between the preform and the mold after contact. The initial temperature of the preform is 100°C. Besides, it should be noted that the internal and the

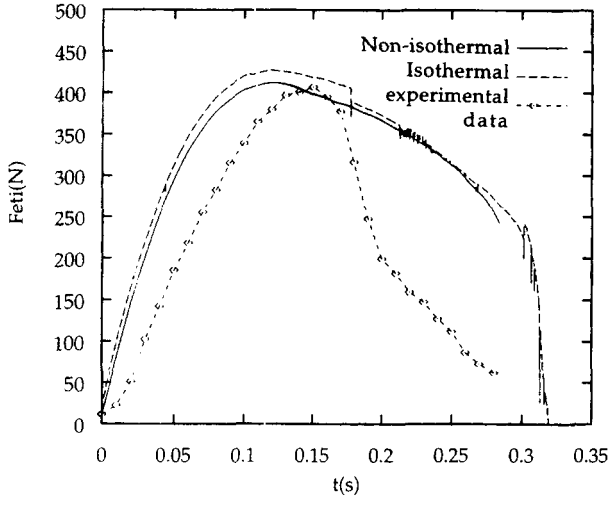

Fig. 18. Measured and computed stretch rod vs. time.

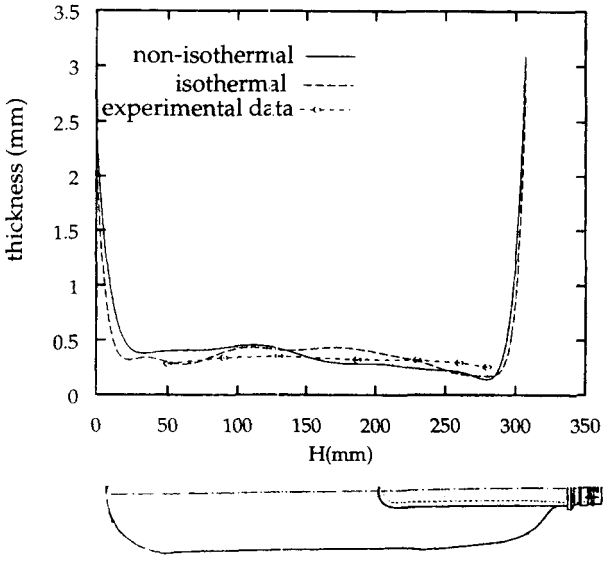

Fig. 19. Thickness distribution at the end of the process.

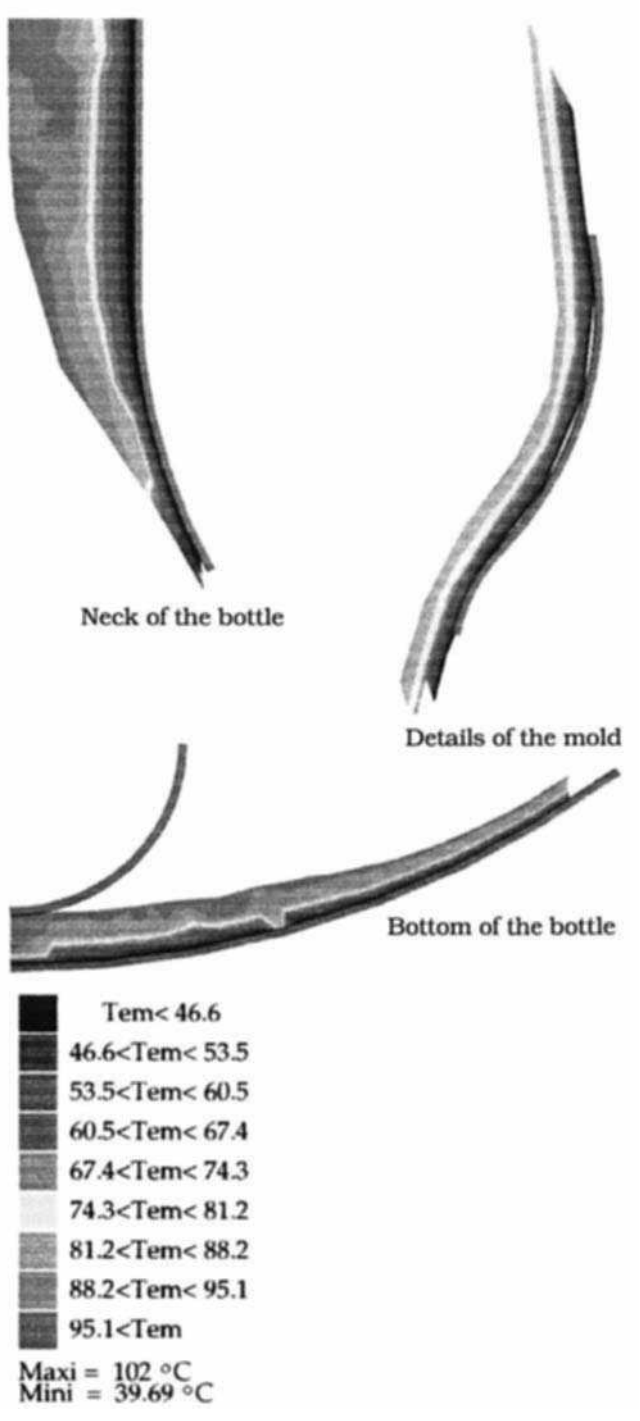

Fig. 20. Temperature distribution at the end of the process.

external heat transfer coefficients are assumed to be the same.

Figure 17 presents intermediate bottle shapes from the beginning to the end of the process. The computed isothermal and nonisothermal stretching force exerted on the stretch rod vs. time are quite equivalent (see *Fig. 18*). This result was expected because heat transfer becomes important only when the outer surface of the preform reaches the inner surface of the mold and on a small area of the bottom of the preform that is in contact with the rod. The nonisothermal stretching force is lower than the isothermal one. This is due to

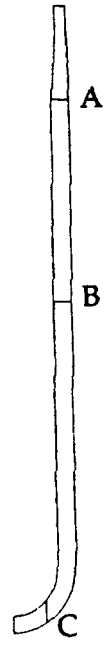

(a)

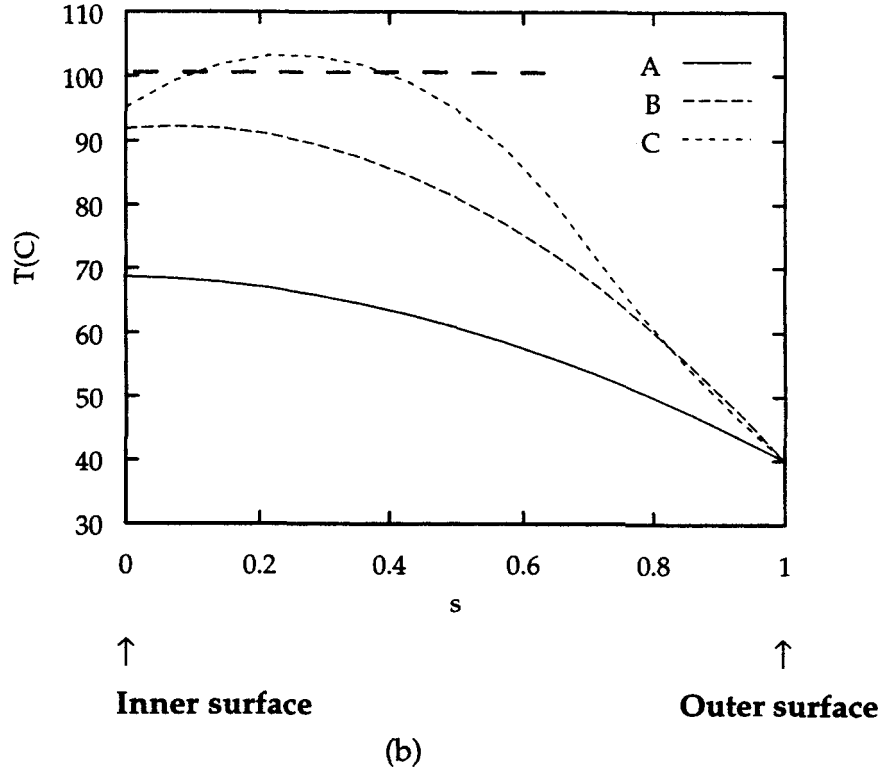

(b)

Fig. 21. Temperature distribution along material lines.

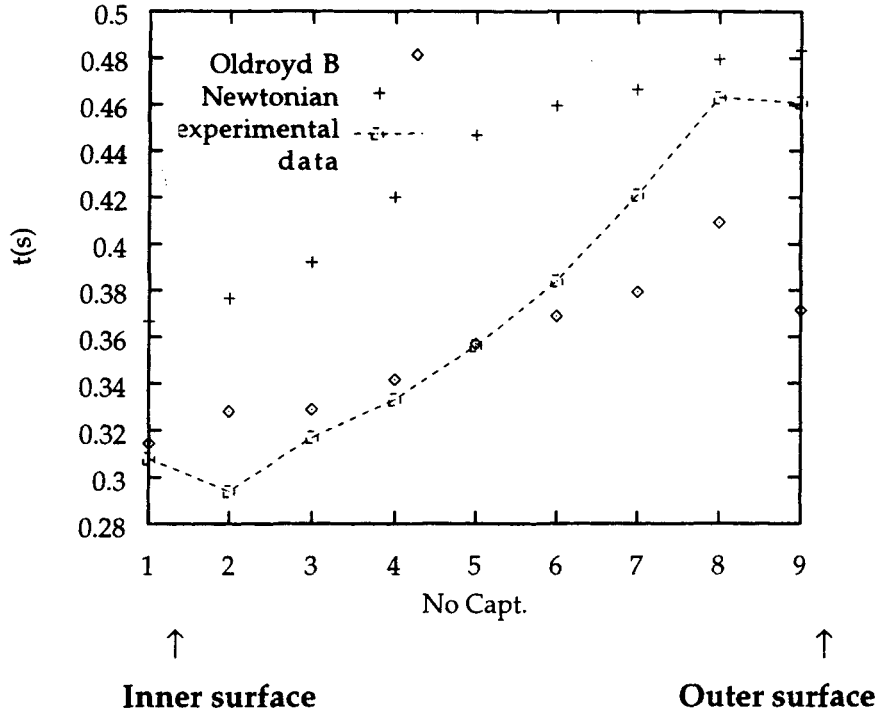

Fig. 22. Comparison of the contact times.

the dissipation energy related to high deformations, which increases the temperature locally. The comparison between the computed thickness distribution and the experimental data at the end of the process is shown in *Fig. 19*. The agreement is better with a non-isothermal model than with an isothermal one.

The temperature distribution at the end of the process is represented in *Fig. 20* at different locations (bottom of the bottle, details of the mold, neck of the bottle). The contact between the stretch rod and the bottom of the preform as well as the contact between the bottle mold and the outer surface of the preform induces high temperature gradients throughout the thickness (maximum 50°C), which justify the volumic approach in order to obtain an accurate description of the temperature distribution. More enlightening is to plot the temperature distribution along three material lines, which are located, respectively, at the neck of the preform (y_A = 290 mm), at the center of the preform (y_B = 250 mm), and at the bottom of the preform (x_c = 6.9 mm) (see *Fig. 21a*). For each material line, the temperature distribution is represented vs. the nondimensional curvilinear coordinate s in the thickness direction (*Fig. 21b*). We note that the temperature increases from the upper material line (A) to the lower one (C). This is due to the expansion of the preform, which occurs from the neck to the bottom of the bottle. So, the contact between the preform and the mold occurs later for line C than for line A. More interesting is that the temperature distribution along line C at the end of the process is partly higher than the initial temperature (see dashed line), which is related to the energy dissipation during inflation. This phenomenon has been observed experimentally.

Contact times versus location of contact sensors for the isothermal model are plotted in *Fig. 22* and compared with experiments. Contact times computed using Oldroyd B model are closer than the Newtonian one. Consequently, it appears that the kinetic of contact (and consequently the kinetic of blowing) depends on the rheological behavior.

6) CONCLUSION

Experiments have been conducted on a well-instrumented stretch blow molding machine: stretching forces as well as contact times between the polymer and the mold have been recorded. The bottle thickness distribution has been measured for various processing parameters.

A coupled model for the thermodynamic of the air and for the thermomechanical inflation of the parison has been proposed. A finite element model and a viscoelastic differential constitutive equation have been used. Viscous dissipation, as well as the temperature gradient between the mold and the molten polymer, has been considered. The comparison between experimental and numerical rod stretching forces is fair. The discrepancy is more important when considering the thickness distribution and the contact kinetic.

Further developments will necessitate a better understanding of the rheology of PET during the stretch blow molding operation (amorphous, i.e., liquid at the beginning of the process, and semicrystalline, i.e., solid at the end of the process).

ACKNOWLEDGMENT

This research was supported by Sidel Company and the French "Ministère de la recherche" (MRT n° 90A 136).

NOMENCLATURE

c_p	heat capacity
$\vec{g}$	gravity
h_a	heat transfer coefficient between air and polymer
h_m	heat transfer coefficient between mold/stretch rod and polymer
$\underline{\underline{I}}$	identity tensor
k	heat conductivity
$\vec{n}$	unit outward normal vector
Nbnoe	number of nodes
p'	arbitrary pressure
$\vec{v}$	velocity field
$\vec{v}^h$	discrete velocity field
$\vec{V}$	assembly of the nodal velocity components
$\vec{P}$	assembly of the nodal pressure vector
$\vec{F}$	assembly of the nodal applied forces
t	time
T	temperature field
$\vec{T}$	assembly of the nodal temperature field
T_m	temperature of the mold
T_a	temperature of the air
$\vec{x}$	coordinate vector
$\vec{x}^h$	discrete coordinate vector
$\vec{x}_n$	coordinate vector at time t_n
$\frac{\delta[.]}{\delta t} = \frac{\partial[.]}{\partial t} + (\vec{v}.\nabla)[.] - \nabla\vec{v}.[.] - [.].^T\nabla\vec{v}$	upper convective time derivative
$\vec{\gamma}$	acceleration field
$\underline{\underline{\dot{\varepsilon}}} = \frac{1}{2}(\nabla\vec{v} + {}^T\nabla\vec{v})$	rate of strain tensor associated with $\vec{v}$
η	total viscosity
η_s	viscous part of the total viscosity
η_v	viscoelastic part of the total viscosity
η_g	viscosity at glass transition temperature
λ	relaxation time
ρ	specific mass
ρ_g	specific mass at glass transition temperature
$\underline{\underline{\sigma}}$	Cauchy stress tensor
$\underline{\underline{\tau}}$	extra-stress tensor
ψ_k	shape functions
Γ	boundary of the domain Ω
Γ_a	part of the boundary Γ that is not in contact with the rod
Γ_m	part of the boundary Γ that is not in contact with the mold
Ω	domain occupied by the preform

REFERENCES

1. P. Lebaudy, *Polymer*, **33**, 1887 (1992).
2. M. D. Shelby, *SPE ANTEC Tech. Papers*, **37**, 1420 (1991).
3. M. R. Kamal, V. Tan, and D. M. Kalyon, *Polym. Eng. Sci.*, **21**, 338 (1981).
4. M. E. Ryan and A. Dutta, *Polym. Eng. Sci.*, **22**, 569 (1982).
5. A. Dutta and M. E. Ryan, *Polym. Eng. Sci.*, **24**, 1232 (1984).
6. W. P. Haessly and M. E. Ryan, *Polym. Eng. Sci.*, **33**, 1279 (1993).
7. M. Cakmak and J. L. White, *J. Appl. Polym. Sc.*, **30**, 3679 (1985).
8. M. K. Warby and J. R. Whiteman, *Comp. Meth. Appl. Mech. Engng.*, **68**, 33 (1988).
9. H. F. Nied, A. Taylor, and H. G. De Lorenzi, *Polym. Eng. Sci.*, **30**, 1314 (1990).
10. K. Kouba and J. Vlachopoulos, "Modeling of Thermoforming and Blow Molding," *Theoretical and Applied Rheology, Proc. XIth Congr. on Rheology*, Brussels, Belgium (August 17–21, 1992).
11. J. M. A. Cesar de Sa, *Engng. Comp.*, Vol. 3, December 1986.
12. K. Chung, *J. Mat. Shap. Tech.*, **7**, N°4, 229 (1989).
13. A. J. Poslinski and J. A. Tsamopoulos, *AIChE J.*, 36, N°12 (December 1990).
14. B. Debbaut, B. Hocq, and J. M. Marchal, *SPE ANTEC Tech. Papers*, **39** (1993).
15. L. Thomas, "Vérification expérimentale d'une thèse sur la modélisation du soufflage avec bi-orientation de bouteilles en P.E.T.," (in French), Report, Ecole des mines de Douai (1991).
16. F. M. Schmidt, J. F. Agassant, M. Bellet, and G. Denis, "Numerical Simulation of Polyester Stretch/Blow Molding Process," Numiform 92, *Proc. 4th Int. Conf. on Numerical Methods in Industrial Forming Processes*, pp. 383–88, Balkema (September 1992).
17. F. M. Schmidt, J. F. Agassant, M. Bellet, and L. Desoutter, *J. Non-Newt. Fluid Mech.*, **64**, 19 (1996).
18. F. M. Schmidt, J. F. Agassant, and M. Bellet, *SPE ANTEC Tech. Papers*, **43**, 817 (1997).
19. M. Zlamal, "Finite Element Methods for Non-Linear Parabolic Equations," R.A.I.R.O. Numerical analysis, Vol. II, n°1, 93 (1977).
20. J. D. Ferry, *Viscoelastic Properties of Polymers*, 3nd Ed., J. Wiley, New York (1980).
21. G. Le Bourvellec, Thesis, in French, Université Pierre et Marie Curie, Paris VI (1984).
22. C. G'Sell, "Instabilités de déformation pendant l'étirage des polyméres solides," in French, *Revue Phys. Appl.*, **23**, 1085 (1988).